Electronic Supplementary Information

ZSM-5-confined Cr_1-O_4 Active Sites Boosting Methane Direct Oxidation to C1 Oxygenates Under Mild Conditions

Mengyu Zeng[a, b,#], Lu Cheng[c,d,#], Qingqing Gu[e,#], Baiyang Yu[a, b], Bing Yang[e], Jing Xu[f], Ying Zhang[a, b], Chengsi Pan[a, b], Xiao-Ming Cao[c, d,*], Yang Lou[a, b,*], Yongfa Zhu[g]

[a]*Key Laboratory of Synthetic and Biological Colloids, Ministry of Education, School of Chemical and Material Engineering, Jiangnan University, Wuxi, Jiangsu 214122, China*

[b]*International Joint Research Center for Photoresponsive Molecules and Materials, Jiangnan University, Wuxi, Jiangsu 214122, China*

[c]*Key Laboratory for Advanced Materials and Feringa Nobel Prize Scientist Joint Research Center, School of Chemistry and Molecular Engineering, East China University of Science and Technology, Shanghai, 200237, China*

[d]*Centre for Computational Chemistry and Research Institute of Industrial Catalysis, East China University of Science and Technology, Shanghai, 200237, China*

[e]*Dalian National Laboratory for Clean Energy, Dalian Institute of Chemical Physics, 457 Zhongshan Road, Dalian, 116023, China*

[f]*School of Food Science and Technology, Jiangnan University, Wuxi, Jiangsu 214122, China*

[g]*Department of Chemistry, Tsinghua University, Beijing 100084, China*

Corresponding authors: yang.lou@jiangnan.edu.cn; xmcao@ecust.edu.cn.

Table of Contents

Supplemental Experimental Section

Fig. S1. XRD pattern profiles of Cr_1/ZSM-5 SAC, Cr/ZSM-5-NP and H-ZSM-5.

Fig. S2. Low-magnification and high-magnification HADDF-STEM images of fresh Cr_1/ZSM-5 SAC.

Fig. S3. Low-magnification (a, b) and atomic (c, d) resolution HAADF-STEM images of used Cr_1/ZSM-5 SAC.

Fig. S4 Representative SEM back-scattering image of used Cr_1/ZSM-5 SAC.

Fig. S5. The spatial distribution and size of the Cr particles in Cr/ZSM-5-NP.

Fig. S6. UV-vis DRS spectra of Cr_1/ZSM-5 SAC, Cr/ZSM-5-NP and pure H-ZSM-5.

Fig. S7. Catalytic performances of the Cr_1/ZSM-5 SAC for DOM at different reaction conditions.

Fig. S8. A typical chromatogram of gas mixtures over Cr_1/ZSM-5 SAC after DOM and standard curve for CO_2 quantification.

Fig. S9. An example ^{1}H-NMR spectrum gained from a typical reaction liquid mixture.

Fig. S10. CH_4 conversion and TOF during DOM on Cr_1/ZSM-5 SAC and Cr/ZSM-5-NP.

Fig. S11. H_2O_2 consumption and Gain Factor during DOM on Cr_1/ZSM-5 SAC, Cr/ZSM-5-NP and H-ZSM-5.

Fig. S12. HAADF-STEM image of Cr_1/ZSM-5 SAC after reaction cycle 5 times.

Fig. S13. The structure of ZSM-5 and Cr_1/ZSM-5 SAC.

Fig. S14. The enumerated single chromium sites for the DFT simulations.

Fig. S15. The spin charge density of $Z[Cr(OH)_2]^+$ (a), $Z[CrO_2]^+$ (b) and $Z[Cr(O)_2(OH)_2]^+$ (c).

Fig. S16. The complete catalytic cycle diagram of DOM by Cr_1/ZSM-5 SAC.

Fig. S17. Raman spectroscopy of fresh Cr_1/ZSM-5 SAC and used Cr_1/ZSM-5 SAC under ambient conditions.

Fig. S18. In situ H_2O_2-DRIFTS spectra on Cr_1/ZSM-5 SAC, Cr/ZSM-5-NP and H-

ZSM-5 at 30 °C.

Table S1. Comparison of catalytic performance for the synthesized catalysts and the reported catalysts in the literature.

Table S2. EXAFS fitting results for Cr_1/ZSM-5 SAC according to the standard crystal model provided by DFT.

Table S3. Apparent activation energy *(E_a)* of Cr_1/ZSM-5 SAC, Cr/ZSM-5-NP and Pure H-ZSM-5.

Table S4. The C1 yield of different Cr/ZSM-5 catalysts.

Table S5. Bader charge analysis of hydroxyl oxygen at different sites.

Table S6. Bader charge analysis of chromium ions in key intermediates.

Supplemental References

Supplemental Experimental section

S1. Materials

Zeolites(ZSM-5) were purchased from Tianjin Yuanli Chemical Co. Deuterium oxide (99.9 atom% D, for NMR) and methanol (≥99.9%) were purchased from Beijing InnoChem Science and Technology Co. Chromium(III) acetate hydroxide (Cr 24% Powder, $Cr_3(OH)_2(OOCCH_3)_7$) was purchased from Alfa Aesar. H_2O_2 (30%), ethylene glycol (AR, 99%) and ethanol absolute (AR, 99%) were purchased from Sinopharm Chemical Reagent Co. 3-(Trimethylsilyl)-1-propane sulfonic acid sodium salt (DSS, 98%) was purchased from TOKYO Chemical Industry Co. Methanol was purchased from concord technology. The high-purity gases (methane, carbon monoxide, carbon dioxide, Argon) used were purchased from Wuxi Xinxiyi Technology Co. Deionized water (18.2 MΩ) was collected from a GWB SERIES apparatus.

S2. Synthesis of Cr single-atom catalysts

The Cr_1/ZSM-5 SACs are prepared via an adsorption method.[1-3] Typically, 224 mg chromium(III) acetate hydroxide ($Cr_3(OH)_2(OOCCH_3)_7$) powder was dissolved in 15ml ethanol (≥99.7%) as precursor solution. 500 mg H-ZSM-5 (SiO_2/Al_2O_3=25, the BET surface area of ca. 310 m^2/g; Tianjin Yuanli Chemical Co) was dispersed with 120 ml ethanol. The diluted Cr precursor solution was then pumped into H-ZSM-5 suspension under the stirring condition. After aging 24 h at room temperature, the obtained powder was dried at 60°C in an oven for 12 h and then calcined in a muffle furnace at 550°C with a heating rate of 5 °C/min in static air. Pure H-ZSM-5 was treated following the same procedure before testing catalytic performance.

S3. Preparation of Cr nanoparticles

In a typical synthesis procedure, chromium acetate hydroxide ($Cr_3(OH)_2(OOCCH_3)_7$) was added to a solution of ethylene glycol ($C_2H_4O_2$) in a three-neck flask under Ar conditions and the system was degassed using a mechanical pump. The mixture solution was then heated to 200 °C for a few minutes and kept at the same temperature for 4h. After cooling to room temperature, well-prepared nanoparticles solution was obtained. The well-prepared nanoparticle solution was then pumped to 500 mg H-ZSM-5 in 120 ml of ethanol absolute solution with constant stirring until the

solution evaporated completely. Then the samples were dried in an oven at 60°C for 12 h and calcined in static air at 550°C for 3 h.

S4. Catalytic performance evaluation

The DOM was carried out in a batch reactor with a total volume of 50 ml. Firstly, the reactor was added to catalysts (10 mg), 0.5 mL H_2O_2 (30%) and 9.5 mL ultrapure water. Next, the reactor was purged 5 times with CH_4 gas and then pressurized to the required pressure (typically 30 bar) with CH_4 gas. The reactor was then heated to the desired temperature (typically 50 °C) and a thermocouple was inserted directly into the solution to measure the temperature. The solution was stirred vigorously at about 1500 rpm/min and kept reacting for the desired time (usually 30 min). After the reaction, the reactor was cooled to below 10 °C in ice-water mixture to minimize the loss of liquid phase products. The gaseous products were collected using gas bags and the total content of CO_2 was analyzed by GC with FID detector by an external standard technique. As shown in a typical GC chromatogram of the gas mixture after the methane oxidation reaction, only CH_4 was detected and almost no CO_2 was produced (Figure S16). The liquid mixture was filtered to remove the catalyst prior to analysis and the obtained liquid phase product was analyzed by ^{1}H-NMR spectroscopy on Bruker AVANCE III HD 400 MHz, and 3-(trimethylsilyl)-1-propanesulfonic acid sodium salt (DSS, 97%; Sigma-Aldrich) was used as a calibration internal standard. During testing, the solvent suppression technique was used to suppress the main water peak signal during NMR measurements. Typically, 700 μl of the liquid phase product solution and 100 μl of D_2O (containing ~0.02% DSS) were mixed and added to the NMR tube. The ^{1}H NMR spectrum of the liquid product after DOM was shown in **Fig. S8**. The positions of this major signal outgoing peaks were DSS (δ = 0.00 ppm), CH_3OH (δ = 3.35 ppm), CH_3OOH (δ = 3.86 ppm), $CH_2(OH)_2$ (δ = 5.04 ppm) and HCOOH (δ = 8.26 ppm). To accurately quantify the content of formed products, their standard curves were established separately. The recoverability of the catalyst was studied for five cycles. The used catalyst was collected by centrifugation, and then the collected catalyst was used for the next cycle of testing.

S5. Catalyst characterization

X-ray powder diffraction (XRD) patterns were collected on a Bruker D8 focus diffraction spectrometer using Cu Kα radiation (1.54056 Å, 40 kV and 40 mA), scanning from 10° to 80° at a speed of 5 °/min.

The X-ray absorption fine structure (XAFS) analyses were used to characterize the local structure and electronic states of synthesized catalyst. Cr K-edge analysis was performed with Si (111) crystal monochromators at the BL11B beamlines at the Shanghai Synchrotron Radiation Facility (SSRF) (Shanghai, China). Before the analysis at the beamline, samples were pressed into thin sheets with 1 cm in diameter and sealed using Kapton tape film. The XAFS spectra were recorded at room temperature using a 4-channel Silicon Drift Detector (SDD) Bruker 5040. Cr K-edge extended X-ray absorption fine structure (EXAFS) spectra were recorded in transmission mode. Negligible changes in the line-shape and peak position of Cr K-edge X-ray absorption near edge structure (XANES) spectra were observed between two scans taken for a specific sample. The XAFS spectra of these standard samples (Cr foil and Cr_2O_3) were recorded in transmission mode. The XANES and EXAFS data were processed and analyzed by the Athena and Artemis software codes.

The amounts of Cr in different catalysts were measured by an inductively coupled plasma optical emission spectrometer (ICP-OES) of Agilent 730 instrument.

High-Angle Annular Dark Field Scanning Transmission Electron Microscopy (HAADF-STEM) images were acquired on a JEM-ARM200F thermal-field emission microscope with a probe Cs-corrector working at 80 kV, as well as the X-ray energy-dispersive spectra (EDS) mappings. Transmission electron microscopy (TEM) images were taken with JEM-2100 instrument at 200 kV. The sample were prepared by dispersing the Cr/ZSM-5 power in ethanol, then one or two drops were added onto copper grids supported on carbon films.

The X-ray photoelectron spectra (XPS) were recorded on a Thermo ESCALAB250Xi spectrometer with an excitation source of monochromatized Al Ka (hv = 1486.6 eV, 150 W) and a pass energy of 30 eV. The values of binding energies were calibrated by the C1s peak of contaminant carbon at 284.80 eV. The data were processed by XPS Peak software.

Thermo Nicolet iS50 FTIR spectrometer with MCT detector and in-situ cell for diffuse reflectance infrared Fourier transform spectroscopy (DRIFTS) studies. The unit contains a temperature-controlled reaction chamber. The sample is heated to 120°C under flowing Ar (30 ml/min) and held for 1 hour. The sample is then rinsed with Ar and purged in Ar gas cooled to room temperature for 30 minutes. Background spectra were collected using Ar at room temperature and the data were reported as Kubelka-Munk spectral corrections. The reaction gas (1% NO/N_2 or H_2O_2-saturated Ar) was then flowed into the cell at a rate of 20 ml/min and IR spectra were taken at a resolution of 4 cm^{-1} for 64 scans. The H_2O_2/NO-DRIFTS experiments were performed at 25 °C. Spectra were acquired every minute during H_2O_2/NO adsorption until the adsorption intensity reached a maximum, then the reaction gas was turned off and changed to Ar (30 ml/min) for desorption for 30 minutes, and the spectra were acquired every minute. All data processing steps were performed using the software package included with the spectrometer.

Raman spectra were obtained with a high-resolution dispersive Raman spectrometer system (HORIBA LabRam HR550) equipped with a 532 nm laser excitation. The laser was focused on the sample by using a focusing microscope equipped with a 50x long working distance Olympus LMPlan 50x/0.35 objective. The LabRam HR spectrometer is optimized for optimal spectral resolution by employing a grating of 1800 grooves/mm (typically about 2 cm^{-1}). The calibration on the Laser Line is to use the 520.7 cm^{-1} silicon wafer to check the wavenumber calibration of the Raman spectrometer. When measuring the Raman spectra, the sample (5-10 mg of loose powder) was placed on a glass slide, then a drop of 30% H_2O_2 was added dropwise to the powder.

S6. Theoretical calculation methods and model construction

To disclose the mechanism of DOM catalyzed by Cr_1/ZSM-5 SAC, the periodic density functional theory calculations were carried out by using Vienna Ab-initio Simulation Package (VASP).[4, 5] The interaction between nuclear and electron was simulated by the projector augmented wave (PAW) method. The cutoff energy for the plane wave was set as 450 eV.[6] The generalized gradient approximation PBE functional

is used to describe the exchange correlation[7] with the modification of van der Waals interaction in zeolite by the DFT-D3(BJ) scheme.[8, 9] All the atoms were relaxed during the geometric optimization. Its convergence criterion was the maximum force on the atom being less than 0.05 eV/Å. The constraint minimization method was used to search the transition state with the same force convergence criterion[10]. It was reported that the molecular entropy confined in the ZSM-5 zeolite pore will lose 38% compared with the free gas molecule.[11, 12] Accordingly, the value was applied to the correction of small molecule entropy of ZSM-5 zeolite. The on-site Coulomb correction of U = 4.0 eV in the framework of Hubbard model was carried out to consider the strong correlation interaction of Cr 3d orbital.[13, 14]

The optimized lattice parameters of ZSM-5 zeolite (**Fig. S13a**) are a = 20.522 Å, b = 20.314 Å, and c = 13.620 Å, which are consistent with the experimental data.[15] Lonsinger and his collaborators have reported that the T12 site is the most stable single Al substitution site in ZSM-5 zeolite[16]. According to EXAFS characterization results, monoatomic Cr was highly dispersed in ZSM-5 zeolite pores. The energetically most stable site for the single Al substitution was adopted as the active site where the chromium species will be anchored. Hence, the Si^{4+} at T12 site, which is located at the intersection of the sine and straight channels of ZSM-5 zeolite, was replaced by the Al^{3+} for metal sub-nanocluster adsorption. The active site of $Z[CrO_2]^+$ (**Fig. S13b**) is identified among the possible single Cr atom sites, which is consistent with the +3 valence state of XANES and XPS results and the 4-fold coordination of EXAFS results (**Table S2**) in ZSM-5 zeolite.

S7. Catalyst stability testing

The stability tests were carried out under the application conditions mentioned in the catalyst testing section. Five cycles were performed with 10 ml of 0.5 M H_2O_2 aqueous solution, 30 bar methane and 10mg of catalyst in a 50ml miniature magnetic autoclave (WCGF model) at 50 °C for 30min. After each reaction, the catalyst was separated from the reaction mixture by centrifugation, filtration and water washing. The collected catalyst was then dried in an oven at 60 °C for 4 hours. Performance tests were performed after each cycle reaction to ensure that sufficient catalyst was available

for the next cycle.

S8. H_2O_2 quantification

The amount of H_2O_2 remaining at the end of a reaction was quantified by titration of aliquots of the final solution against acidified $Ce(SO_4)_2$ solution using the Ferroin indicator.

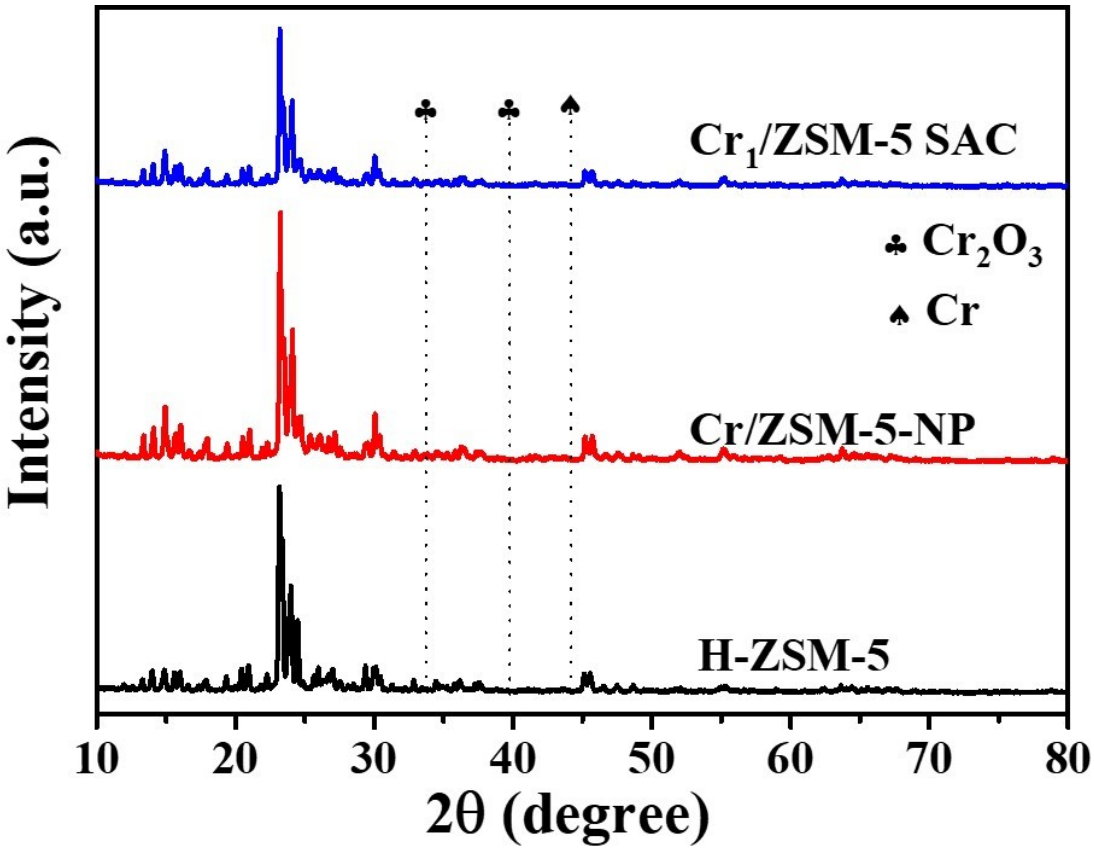

Fig. S1. XRD pattern profiles of Cr_1/ZSM-5 SAC, Cr/ZSM-5-NP and H-ZSM-5.

There are no any characteristic peaks of Cr (44.1°) or Cr_2O_3 particles (33.8 and 39.8°) that can be observed from XRD patterns of Cr_1/ZSM-5 SAC and Cr/ZSM-5-NP, which indicates Cr species are highly dispersed on H-ZSM-5. In addition, XRD pattern profiles of Cr_1/ZSM-5 SAC and Cr/ZSM-5-NP show no observable difference compared with pure H-ZSM-5, indicating that the presence of Cr species does not change the lattice structure of H-ZSM-5.

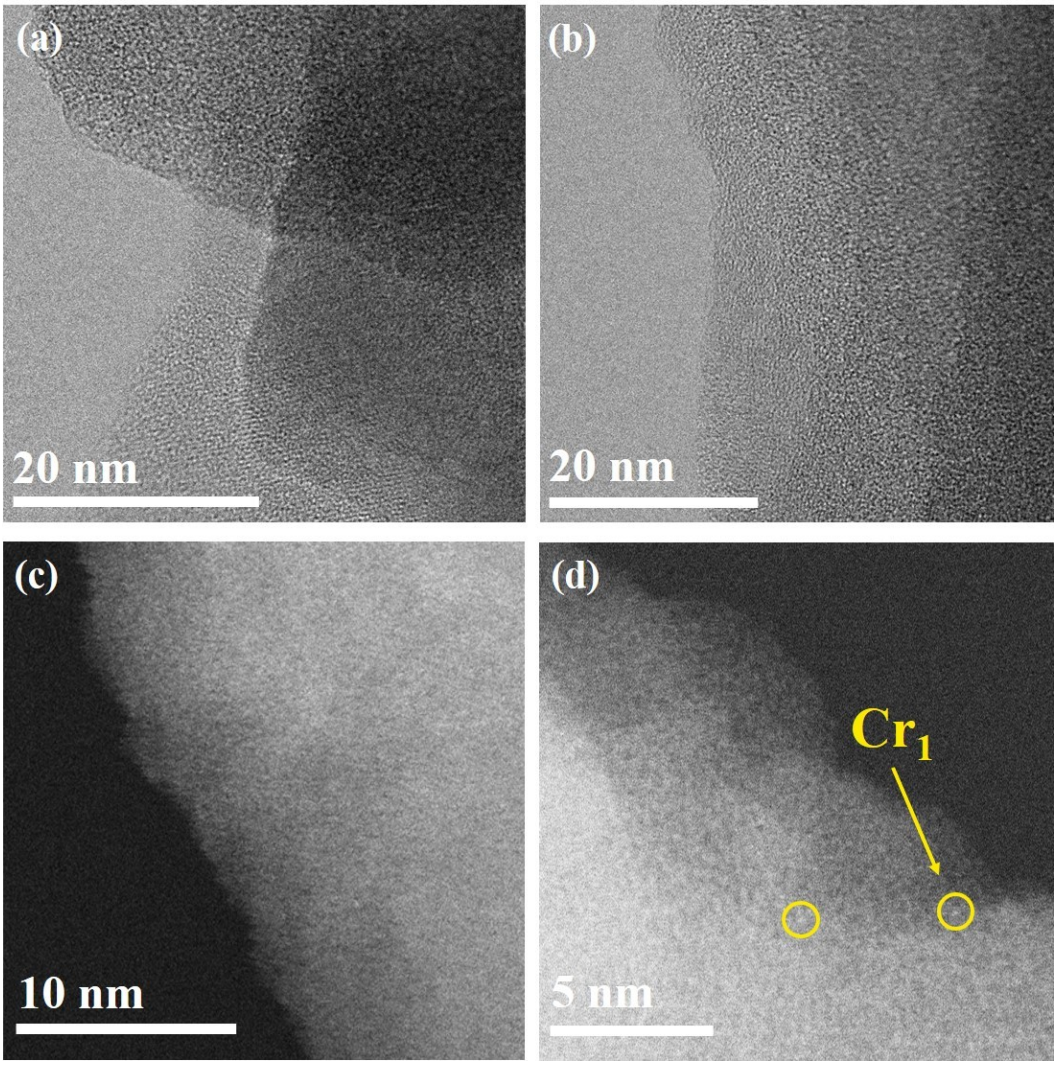

Fig. S2. Low-magnification and high-magnification HAADF-STEM images of fresh Cr_1/ZSM-5 SAC.

As clearly shown in the HAADF-STEM images, isolated Cr atoms are uniformly dispersed on fresh Cr_1/ZSM-5 SAC. High-magnification HAADF-STEM images confirm the absence of any nano particles in the fresh Cr_1/ZSM-5 SAC. Moreover, single atoms can be clearly observed from atom-resolution image (yellow circle). By examining numerous HAADF-STEM images obtained from different regions of the catalyst samples, we unambiguously conclude that Cr species are atomically dispersed in the fresh Cr_1/ZSM-5 SAC.

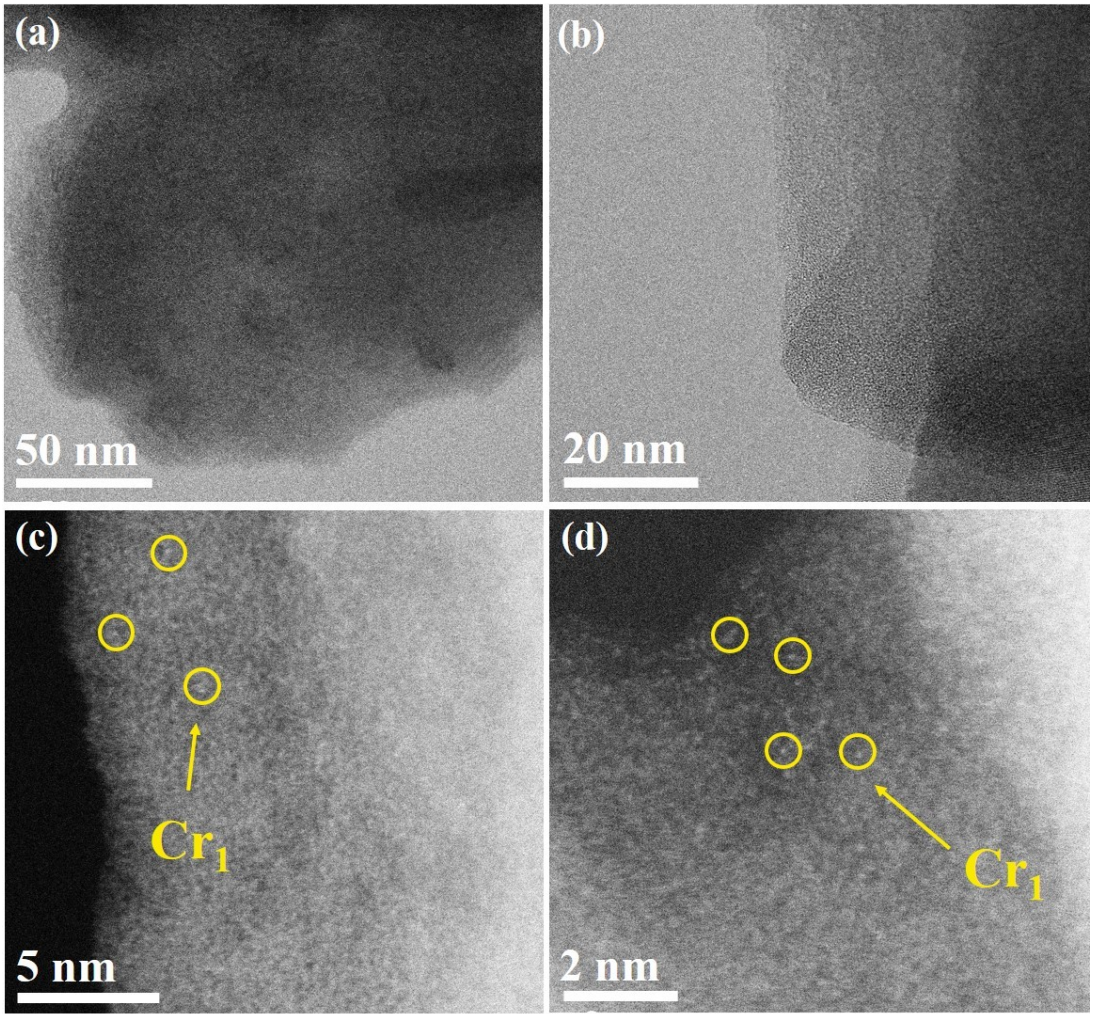

Fig. S3. Low-magnification (a, b) and atomic (c, d) resolution HAADF-STEM images of used Cr_1/ZSM-5 SAC.

As clearly shown in Fig. S3, isolated Cr atoms are uniformly dispersed on used Cr_1/ZSM-5 SAC (30 bar CH_4 for 30 min at 50 ^oC, details in experimental section). Low/High-magnification HAADF-STEM images confirm the absence of any nano particles in the used Cr_1/ZSM-5 SAC. Moreover, single Cr atoms can be observed from atom-resolution image (yellow circle). The atomically dispersed Cr species are still retained and no Cr clusters and nanoparticles are observed, which reveals that the single Cr atoms are stably anchored on the ZSM-5 and secures that the measured catalytic activity original from the single atoms rather than the clusters or particles.

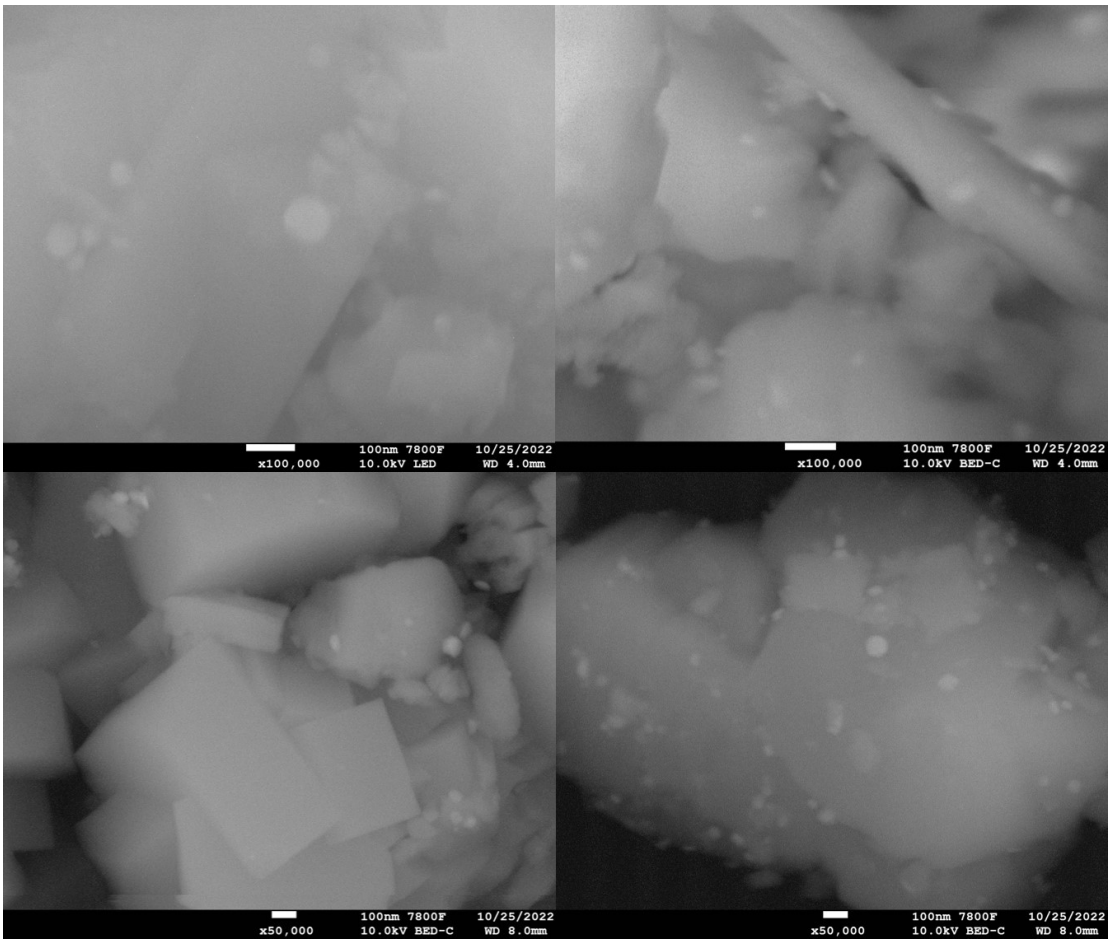

Fig. S4. Representative SEM back-scattering image of used Cr_1/ZSM-5 SAC.

As shown in the SEM back-scattering images, there are no Cr particles present on the surface of ZSM-5 since any Cr particles, if present, will show bright dots due to the strong contrast.

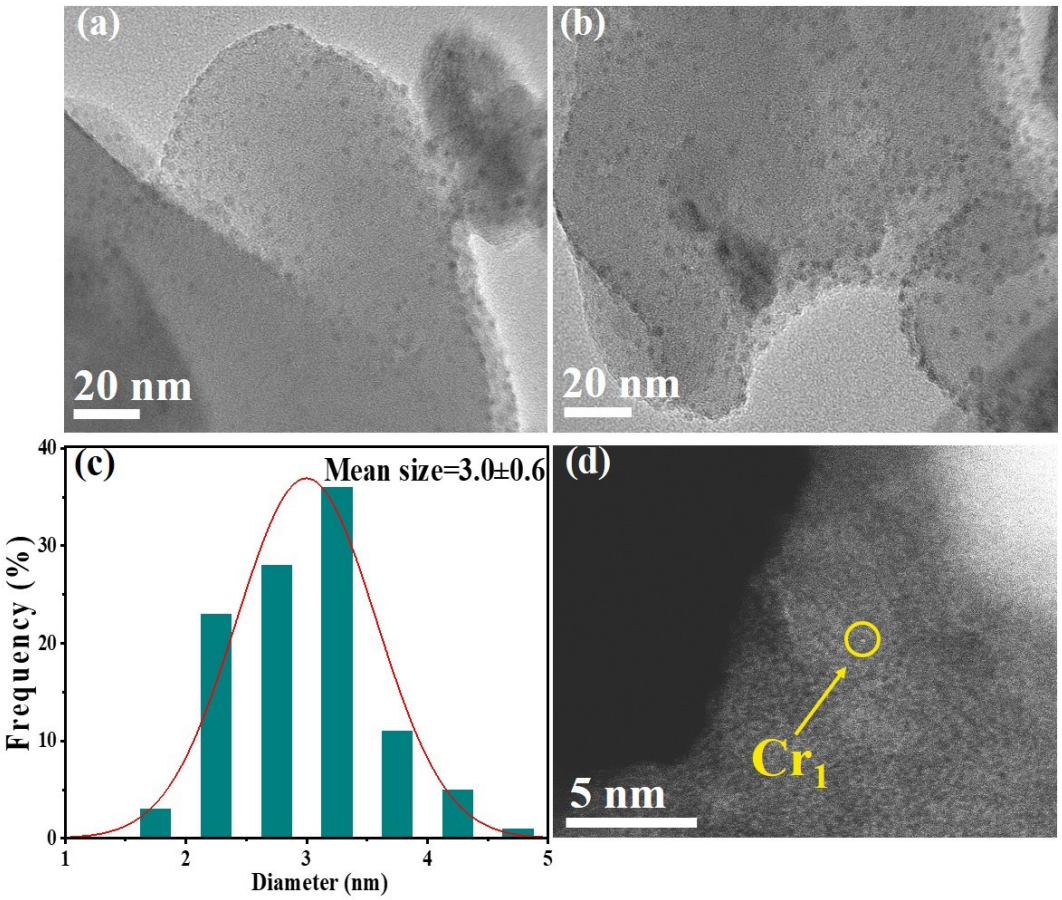

Fig. S5. The spatial distribution and size of the Cr particles in Cr/ZSM-5-NP. TEM (a-b), size distribution (c) images of Cr/ZSM-5-NP and HAADF-STEM (d) images of Cr_1/ZSM-5 SAC.

The number and size of Cr nanoparticles were calculated using particle size distribution software. The average size of Cr nanoparticles dispersed onto the ZSM-5 is 3.0 ± 0.6 nm. Meanwhile, there are still some isolated Cr atoms present on the ZSM-5.

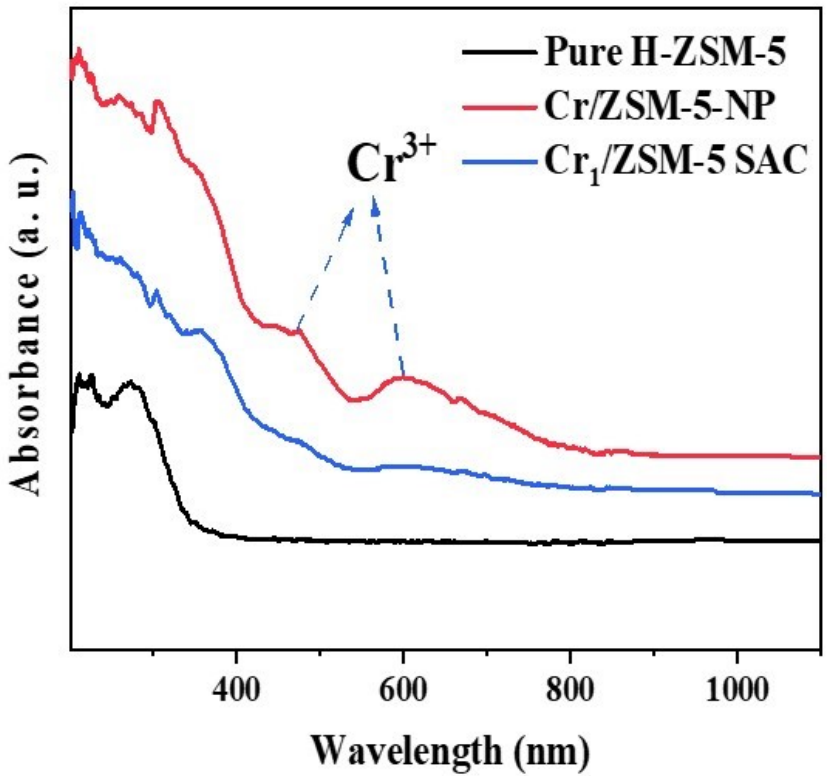

Fig. S6. UV−vis DRS spectra of Cr_1/ZSM-5 SAC, Cr/ZSM-5-NP and pure H-ZSM-5.

For the Cr/ZSM-5 NP, the broad absorption bands at ~458 nm and ~600 nm are associated with the A_{2g}-T_{1g} and A_{2g}-T_{2g} transitions of Cr(III) in octahedral symmetry respectively, which is the typical characteristic absorption band of the octahedral Cr^{3+} species in CrO_x clusters or Cr_2O_3.[17-19] The absence of such absorption band in the Cr_1/ZSM-5 SAC indicates that the Cr species are atomically dispersed on the ZSM-5.

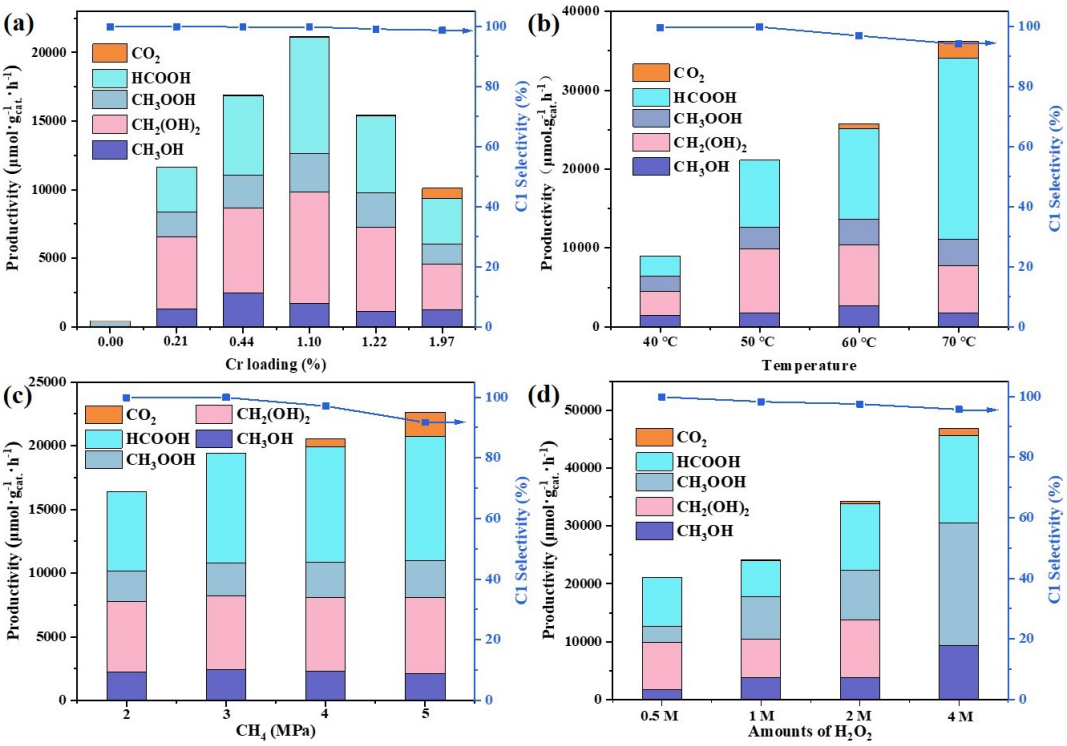

Fig. S7. Catalytic performances of the Cr_1/ZSM-5 SAC for DOM at different reaction conditions. (a) Catalytic performances of Cr/ZSM-5 with different Cr loading for DOM. (Conditions: 10 mg catalyst, P = 3 MPa, 0.5 M H_2O_2, T = 50 °C, t = 0.5 h). (b) Effects of reaction temperatures (Conditions: 10 mg catalyst, P = 0.5 MPa, 0.5 M H_2O_2, t = 0.5 h). (c) Effects of the initial methane pressure (Conditions: 10 mg catalyst, 0.5 M H_2O_2, T = 50 °C, t = 0.5 h). (d) Effects of the amounts of H_2O_2 (Conditions: 10 mg catalyst, P = 3 MPa, T = 50 °C, t = 0.5 h).

By optimizing the DOM reaction conditions including Cr loading, temperature, methane pressure and amounts of H_2O_2, the highest catalytic performance was achieved for Cr_1/ZSM-5 SAC at 3 MPa and 50 °C under the reaction conditions of 0.5 M H_2O_2.

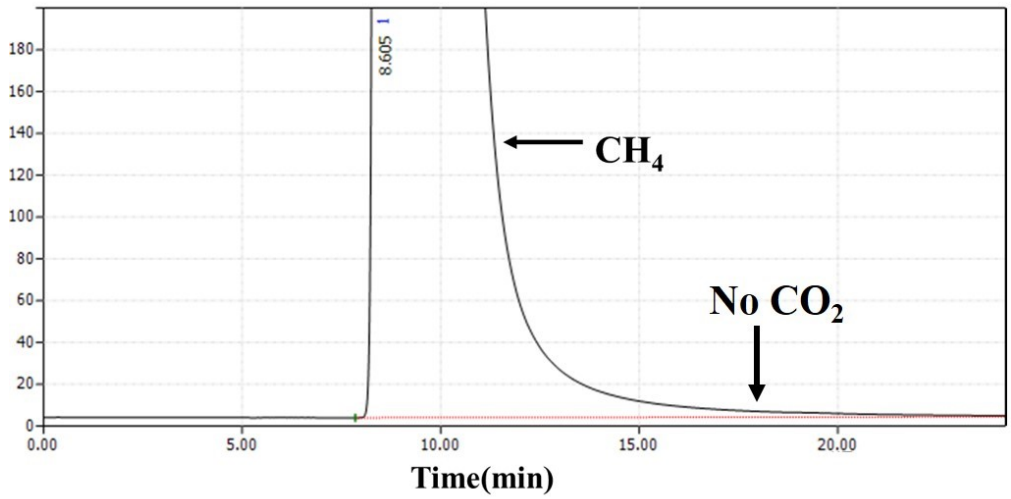

Fig. S8. A typical chromatogram of gas mixtures over Cr_1/ZSM-5 SAC after DOM and standard curve for CO_2 quantification.

An example of Chromatography is gained from a typical reaction gas mixture.

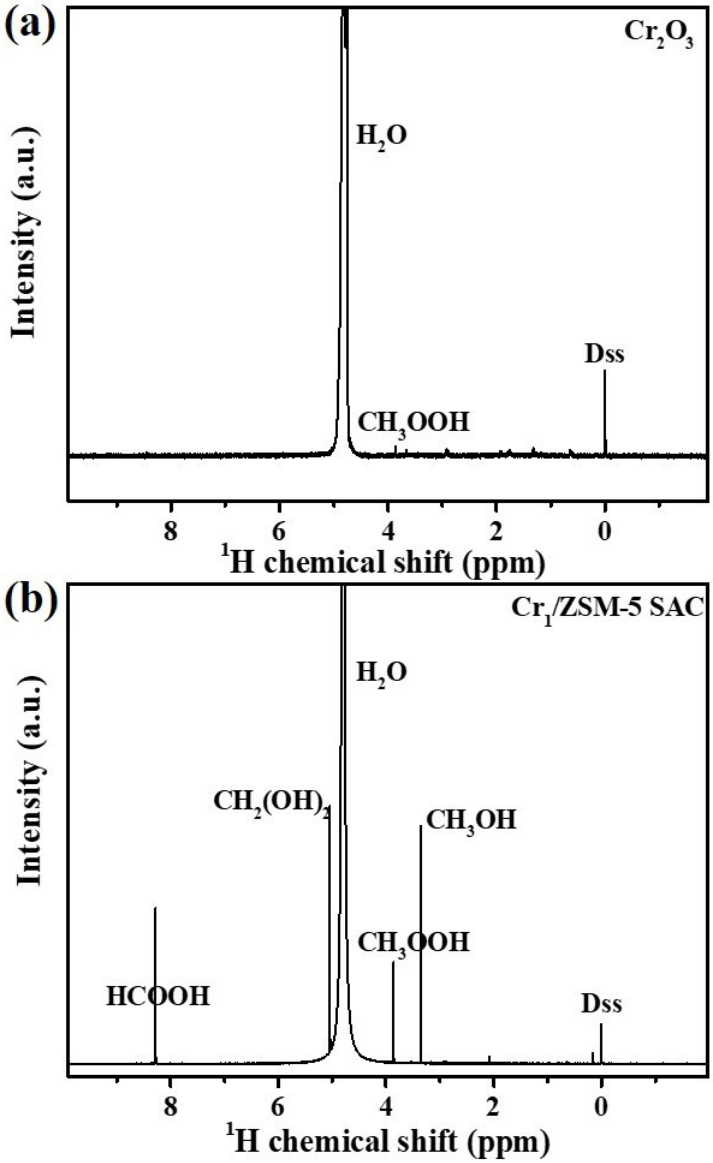

Fig. S9. An example ^{1}H-NMR spectrum gained from a typical reaction liquid mixture. Commercial Cr_2O_3 catalyst (a) and Cr_1/ZSM-5 SAC (b). Reaction conditions: 10 mg catalysts, 0.5 mL H_2O_2 (30%), 9.5 mL deionized water, 3 MPa CH_4, in a stainless-steel autoclave with a Teflon liner vessel at 50°C for 0.5h.

As shown in Figure S9, Cr_2O_3 only displays weak signal peaks of CH_3OOH, CH_3OH and DSS internal standard. The oxygenated species are CH_3OH (δ = 3.35 ppm), CH_3OOH (δ = 3.86 ppm), $CH_2(OH)_2$ (δ = 5.04 ppm) and HCOOH (δ = 8.26 ppm) by Cr_1/ZSM-5 SAC. DSS (δ = 0.00 ppm) is used as an internal standard.

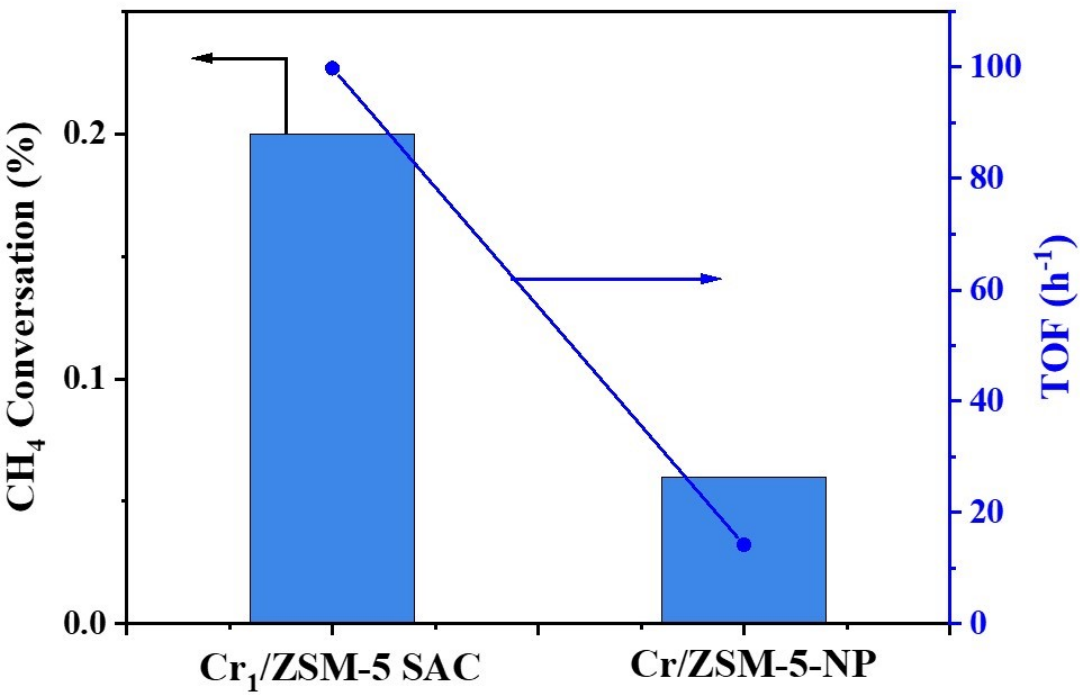

Fig. S10. CH_4 conversion and TOF during DOM on Cr_1/ZSM-5 SAC and Cr/ZSM-5-NP.

Reaction Condition: 10 mg catalysts dispersed in 10 ml of 0.5 M H_2O_2 aqueous solution, 30 bar CH_4 for 30 min at 50 °C.

The methane conversion (%) is calculated as:

$$\text{CH4 conversion (\%)} = \frac{\text{Total prodcuts (μmol)}}{\text{Initial methane (μmol)}} \times 100 \quad (1)$$

Turnover frequency (TOF) is defined as:

$$\text{TOF} = \frac{\text{C1 oxygenates * (μmol)}}{\text{Loading of Cr (μmol)} \times \text{reaction time (h)}}$$

* The amounts of C1 oxygenates are the amount produced by the Cr_1/ZSM-5 SAC minus the amount of oxidation products formed by pure H-ZSM-5.

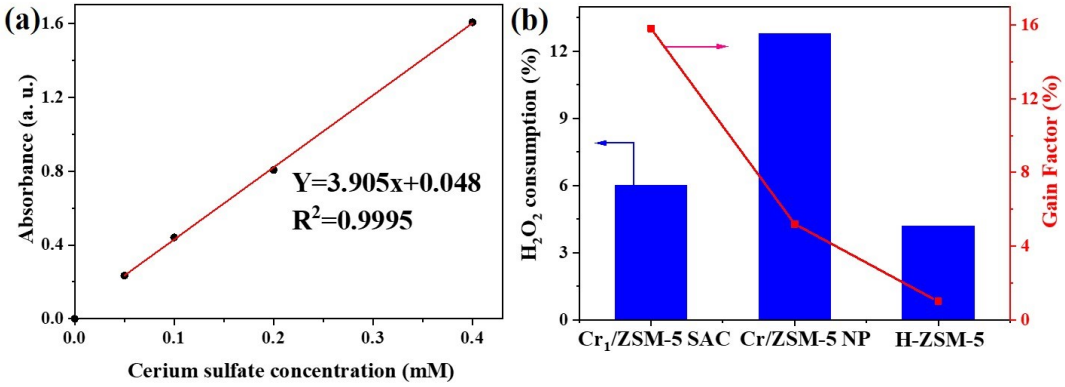

Fig. S11. H_2O_2 consumption and Gain Factor during DOM on Cr_1/ZSM-5 SAC, Cr/ZSM-5-NP and H-ZSM-5 (a) The absorption values of different concentrations of cerium sulfate were tested to the standard curve using UV-vis spectroscopy, and the wavelength (λ) used for the measurements was 316 nm. (b) H_2O_2 consumption and Gain Factor during DOM on Cr_1/ZSM-5 SAC, Cr/ZSM-5-NP and H-ZSM-5. Reaction Condition: 10 mg catalysts sample dispersed in 10 ml of 0.5M H_2O_2 aqueous solution, 30 bar CH_4 for 30 min at 50 ℃.

H_2O_2 consumed was assayed by the titanium oxalate spectrophotometric method.
A gain factor is defined as:
Gain factor = C1 oxygenates (μmol)/H_2O_2 consumption (μmol)

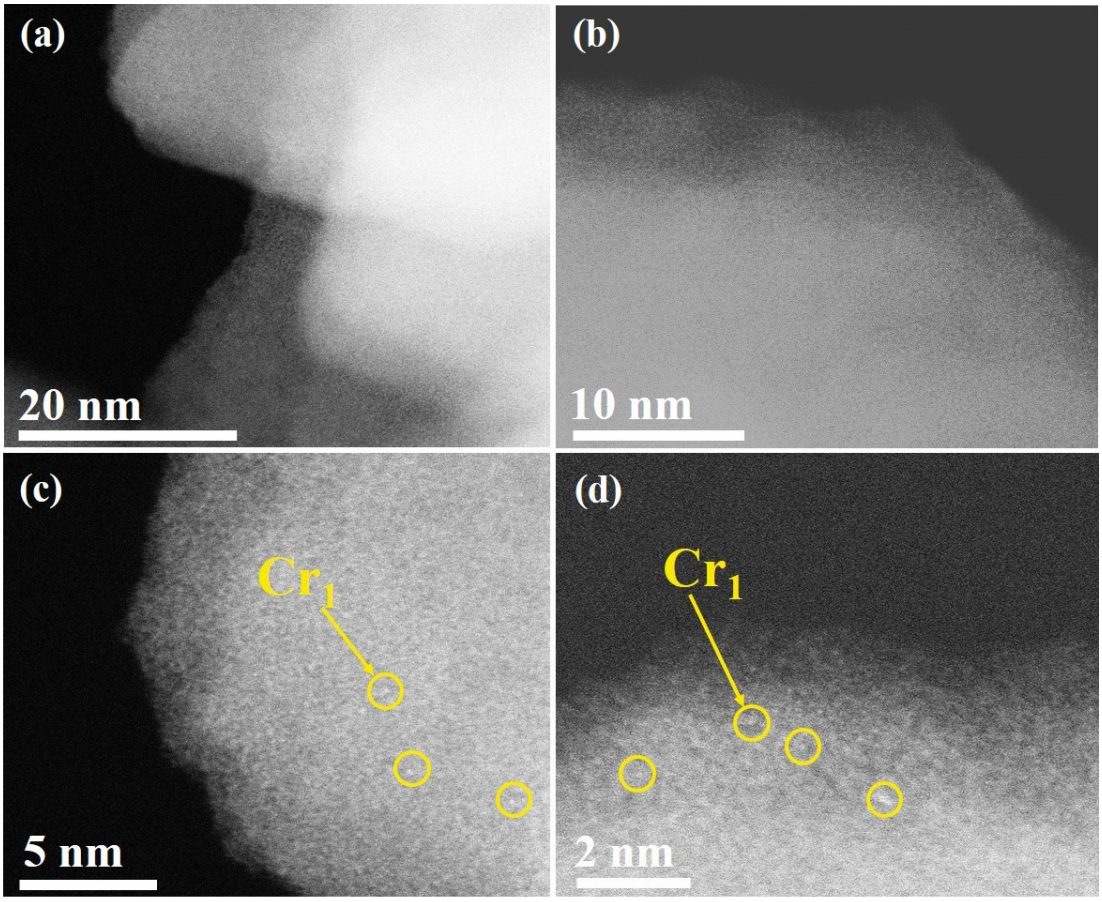

Fig. S12. HAADF-STEM image of Cr_1/ZSM-5 SAC after reaction cycle 5 times.

After five cycles of DOM over Cr_1/ZSM-5 SAC, no obvious clusters and nanoparticles were observed. Alternatively, the presence of isolated Cr_1 atoms observed at high-magnification HAADF-STEM images indicates a stable anchoring of the Cr_1 atoms to ZSM-5, which assures that the measured catalytic performance is original from the isolated Cr atoms rather than the Cr clusters or particles.

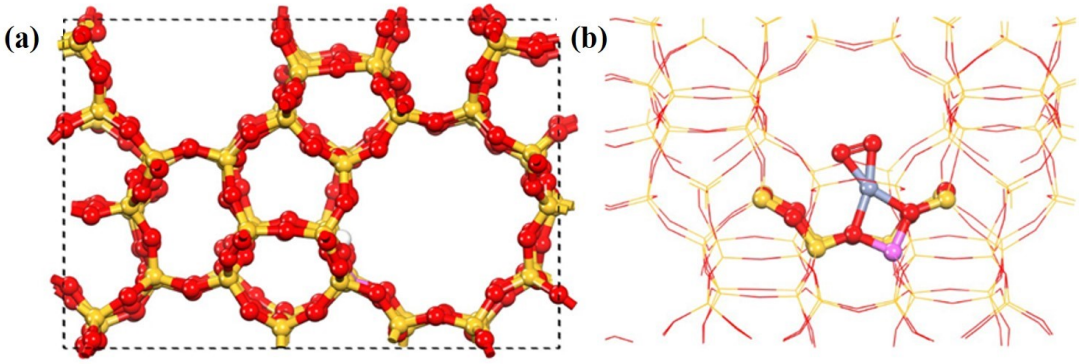

Fig. S13. The structure of ZSM-5 and Cr_1/ZSM-5 SAC. The Structure of ZSM-5 (a); The local optimized structure of Cr_1/ZSM-5 SAC (b).

The optimized structure of the Cr_1/ZSM-5 catalyst is constructed according to the XRD, HAADF-STEM, EDS mapping, and EXAFS data. The local optimization of the active structure shows that chromium single atom is adsorbed at the T12 site of γ-8MR in ZSM-5 zeolite.

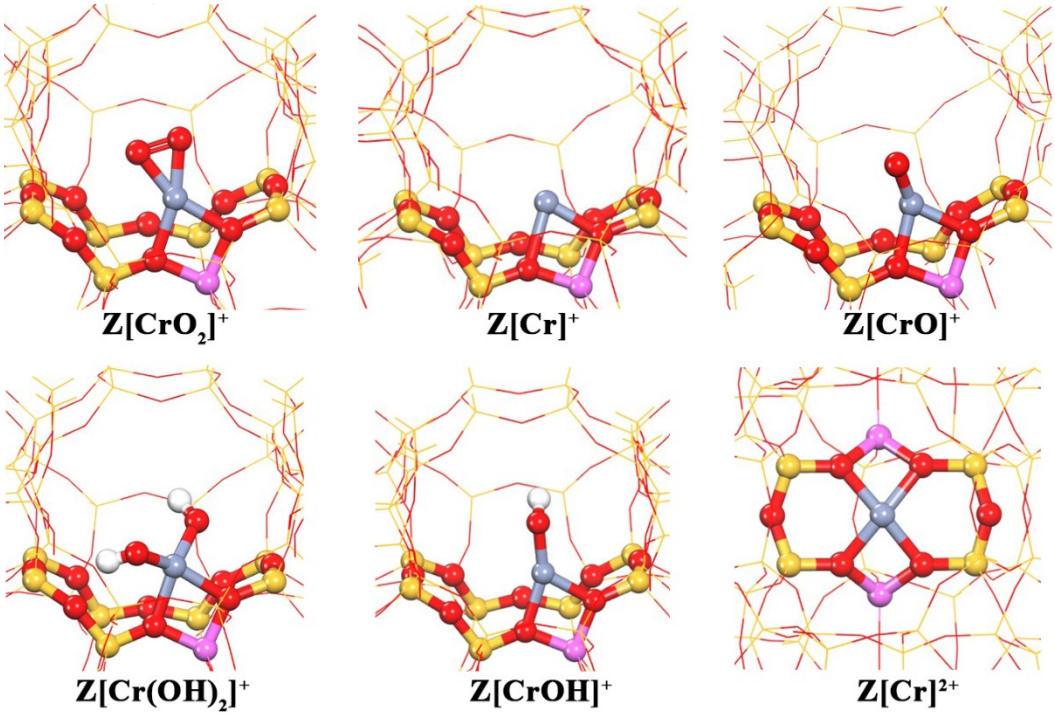

Fig. S14. The enumerated single chromium sites for the DFT simulations. The H, O, Si, Al, and Cr atoms of the reaction sites are displayed in white, red, yellow, pink, and blue in the ball and stick style, respectively. The display settings were kept throughout the whole paper.

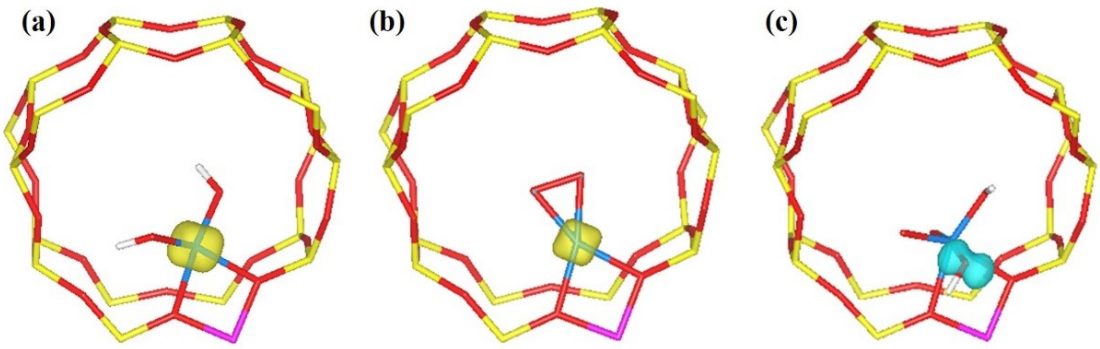

Fig. S15. The spin charge density of $Z[Cr(OH)_2]^+$ (a), $Z[CrO_2]^+$ (b) and $sZ[Cr(O)_2(OH)_2]^+$ (c).

Due to the strong electron-donating ability of Cr species, no spin could be found for both hydroxyls at the Cr sites of $Z[Cr(OH)_2]^+$, indicating the formation of OH^- (**Fig. S15a**).For $Z[CrO_2]$, negligible spin is found for the O_2 and the O-O bond length is 1.424 Å, indicating that the peroxide O_2^{2-} is formed. Since $[CrO_2]$ needs to compensate a charge to the skeleton of the zeolite, the trivalent Cr would exist at $Z[CrO_2]^+$. The spin charge density analysis of $Z[Cr(O)_2(OH)_2]^+$ discloses the formation of hydroxyl radicals at hexavalent Cr center. It is further confirmed by the Bader charge of hydroxyl oxygen (**Table S4**). The hydroxyl radical possesses a high reactivity and is easy to activate the C-H bond of methane, which is one of the main reasons for the high activity of Cr_1/ZSM-5 SAC.

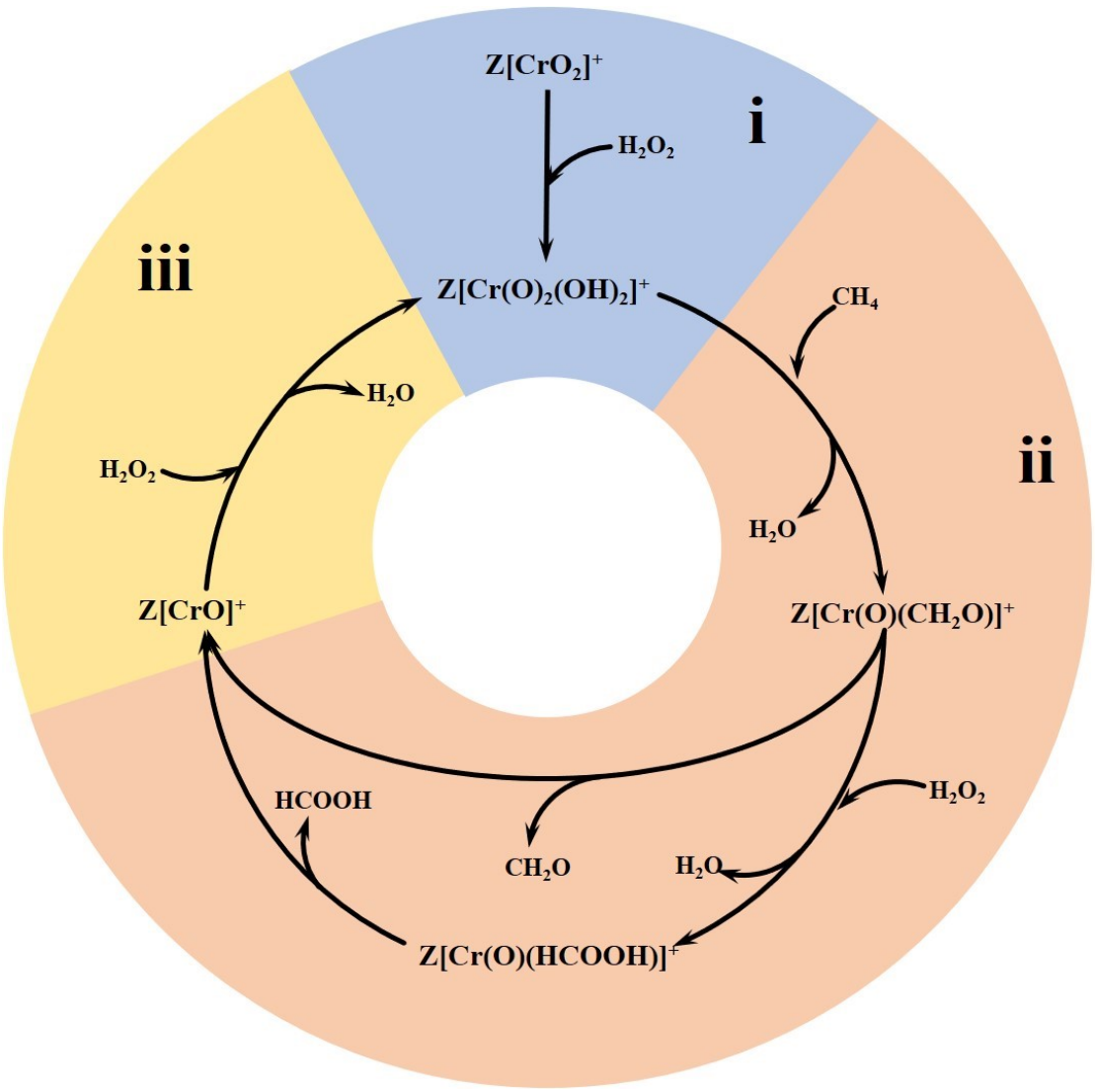

Fig. S16. The complete catalytic cycle diagram of DOM by Cr_1/ZSM-5 SAC.

DFT theoretical calculation proves that the reaction mechanism of methane oxidation by Cr_1/ZSM-5 SAC can be divided into three steps: (i) the pre-activation of reaction site, (ii) oxidation of methane, and (iii) regeneration of active sites.

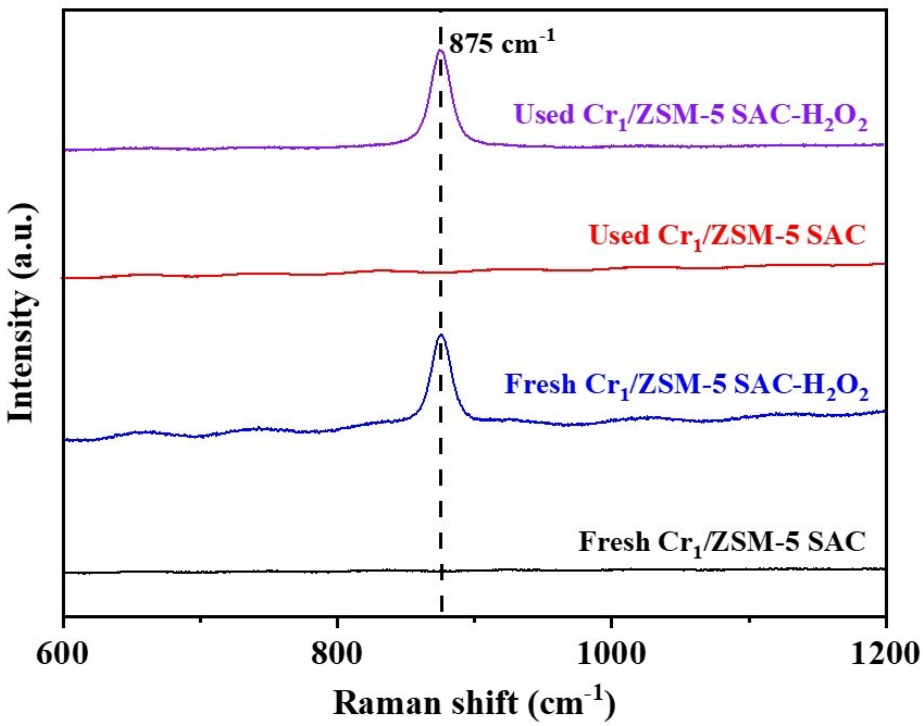

Fig. S17. Raman spectroscopy of fresh Cr_1/ZSM-5 SAC and used Cr_1/ZSM-5 SAC under ambient conditions.

To further verify the electronic state of active site in DOM simulated by the DFT calculations, the oxidation state of Cr species in fresh and used Cr_1/ZSM-5 SACs was probed by the Raman spectra. It was difficult to observe Cr^{3+} species on the Raman spectroscopy because of the forbidden ligand field transitions in the visible region of the supported low-valent chromium ions, which leads to the absence of Raman signal on the fresh Cr_1/ZSM-5 SAC sample.[20, 21] It is consistent with the XPS, XANES and in-situ NO-DRIFTS data that the oxidation state of Cr_1 species primarily present as +3. Nevertheless, after dropping H_2O_2 on the fresh Cr_1/ZSM-5 SAC, the peak centered at 875 cm^{-1} associated with the symmetric stretching modes of O-Cr-O of mononuclear Cr^{6+} species was observed[22-24], which reveals that the electronic state of Cr species has been oxidized to Cr^{6+} from Cr^{3+}. It is consistent with the oxidation state of Cr species in the active site of $Z[Cr(O)_2(OH)_2]^+$ **(IM4)** simulated by the DFT calculation. For the used Cr_1/ZSM-5 SAC before dropping H_2O_2, the characteristic peak centered at 875 cm^{-1} disappeared, which indicates that the mononuclear Cr^{6+} species has been reduced during the catalytic process of DOM. However, after dropping the H_2O_2 onto the used Cr_1/ZSM-5 SAC, the characteristic peak centered at 875 cm^{-1} appeared again, which

indicates that the Cr species in the used Cr_1/ZSM-5 SAC has been re-oxidized to Cr^{6+} species. Those results indicate that the presence of H_2O_2 enables to efficiently oxidize the Cr^{3+} species to active Cr^{6+} species, which boosts the catalytic process of DOM over Cr_1/ZSM-5 SAC.

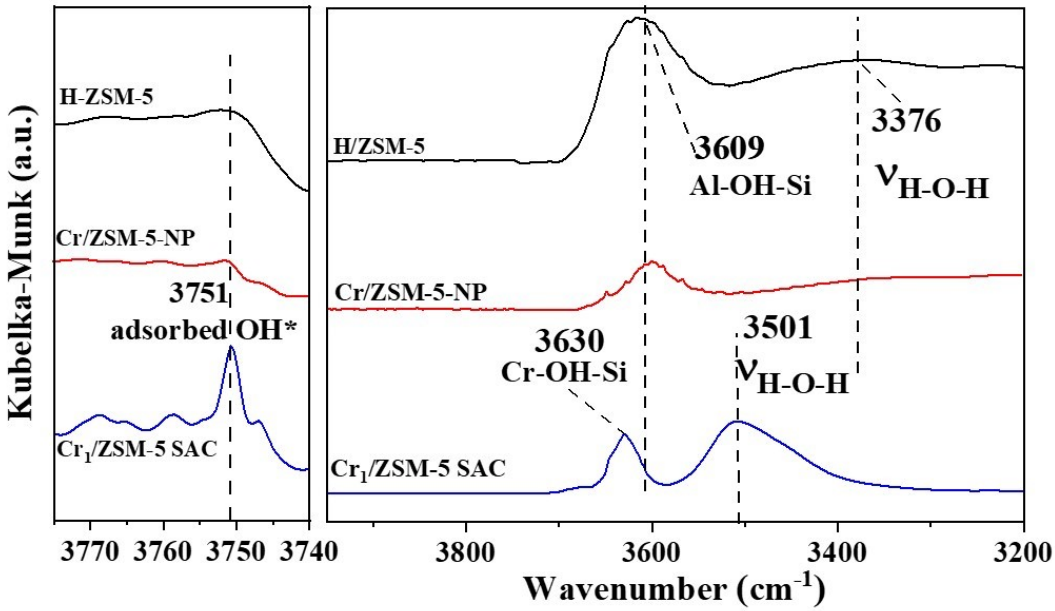

Fig. S18. In situ H_2O_2-DRIFTS spectra on Cr_1/ZSM-5 SAC, Cr/ZSM-5-NP and H-ZSM-5 at 30 °C.

For the adsorption of H_2O_2 on Cr_1/ZSM-5 SAC sample, there are two prominent absorption bands at approximately 3630 and 3501 cm^{-1} associated with the bridging hydroxyl groups (Cr-OH-Si) and OH stretching $\upsilon(H_2O)$, respectively, appearing upon the introduction of H_2O_2 as shown in Figure S13. Moreover, the band at 3751 cm^{-1} was observed, which is associated with the surface-adsorbed OH*.[25] However, for the adsorption of H_2O_2 on Cr/ZSM-5-NP and H-ZSM-5, the peak at 3609 cm^{-1} associated with the bridged Al-OH-Si species is observed.[26] Alternatively, no significant OH* adsorption was observed on the Cr/ZSM-5-NP and H-ZSM-5, further revealing that the formation of adsorbed hydroxyl groups was promoted on Cr_1 atoms.

Table S1. Comparison of catalytic performance for the synthesized catalysts and the reported catalysts in the literature.

Catalyst	C1 selectivity（%）	Products amounts（μmol）					Yield	Reaction conditions					Refs
		CH_3OH	CH_3OOH	$CH_2(OH)_2$	HCOOH	CO_2	($mmol.g^{-1}.h^{-1}$)	Time (h)	P (MPa)	T (℃)	H_2O_2 (M)	Catalyst (mg)	
Cr_1/ZSM-5 SAC	99.8	8.7	40.5	13.9	42.5	0.2	21.10	0.5	3	50	0.5	10	This work
Cr_2O_3	85.2	0.67	1.43	0	0	0.37	0.42	0.5	3	50	0.5	10	
Cr/ZSM-5-NP	96.8	5.53	12.48	12.43	5.81	1.2	7.25	0.5	3	50	0.5	10	
Cu-Fe/ZSM-5	85.0	188.8	0.5	0	0	33.3	14.02	0.5	3.05	50	0.5	27	27
$CuPdO_2$/CuO	93.9	40.8	10.6				5.47	1	3	50	0.5	10	28
1%AuPd/TiO_2	90.0	0.29	1.12	0	0	0.16	0.28	0.5	3	50	0.5	10	29
AuPd colloid	93.5	3.3	11.8	0	0.6	1.1	0.31	0.5	3	50	0.1	100	30
Cr_1/TiO_2	93.0	3.4	17.5	20.8	2.2		4.39	1	3	50	0.5	10	31
0.1%Fe/ZSM-5	97.1	177	248	191	431	31	6.98	0.5	3	50	0.5	300	32
Cu_1/ZSM-5	99						9.6	0.5	3	50	0.5	28	33
Cu_2@C_3N_4-D2		91	611	4176	0		4.88	1	3	50	0.5	50	34
0.01%Pd_1O_4/ZSM-5	96.2	7.39	39.48	0	60.82	4.22	7.69	0.5	3	50	0.5	28	35
Rh_1/ZrO_2	78.8	0.94	0.21	0	0	0.31	0.08	0.5	3	70	0.5	30	36
FeN4/GN	94.0	5.6	41.4	32.5	35.5	300	0.23	10	2	25	5	50	37
AuPd/TiO_2	88.4	1.84	6.39	0	0	1.08	0.59	0.5	3.05	90	0.5	28	38

Table S2. EXAFS fitting results for Cr_1/ZSM-5 SAC according to the standard crystal model provided by DFT.

Sample	Path	CN	R_{fit} (Å)	R_{real} (Å)	σ^2 (Å^2)	R-factor	ΔE (eV)
Cr_1/ZSM-5 SAC	Cr-O_{Dual}	2	1.9255	1.872	0.00066	0.019	-3.2
	Cr-O_{FM}	2	1.9912	2.058	0.00004		

CN is the coordination number; R_{fit} is fitting distance; R_{real} is real distance in the model provided by DFT calculation; σ^2 is Debye-Waller factor.

Table S3. Apparent activation energy (E_a) of Cr_1/ZSM-5 SAC, Cr/ZSM-5-NP and pure H-ZSM-5.

Sample	Apparent activation energy[a] kJ/mol
H-ZSM-5	139.3
Cr/ZSM-5-NP	57.6
Cr_1/ZSM-5 SAC[b]	45.8

[a] Measured at 30 bars CH_4 and 0.5 M H_2O_2. Between 40 °C and 70 °C with a 10 °C increment.
[b] Prepared with organometallic precursor $Cr_3(OH)_2(OOCCH_3)_7$.

Table S4. The C1 yield of different Cr/ZSM-5 catalysts.

Entry	Sample	Cr content(wt.%)	C1 product ($\mu mol.g_{cat}^{-1}$)
1	Pure H-ZSM-5	0.0007	216
2	Cr/ZSM-5-NP	1.33	3624.5
3	Cr_1/ZSM-5 SAC	1.10	10560
4	1Cr/ZSM-5	0.44	8435
5	2Cr/ZSM-5	1.22	7700
6	3Cr/ZSM-5	1.97	6335

Table S5. Bader charge analysis of hydroxyl oxygen at different sites.

Site	Bader charge/|e|	HO species [a]
$Z[Cr(OH)_2]^+$	-1.09	HO^-
$Z[Cr(OH)_4]^+$	-1.07	HO^-
$Z[CrO_2(OH)_2]^+$	-1.19	HO^-
$Z[Cr(O)_2(OH)_2]^+$	-1.18/-0.81	HO^-/ $HO\cdot$
H_2O_2	-0.62	$HO\cdot$
H_2O	-1.12	HO^-

[a] The valence state of the hydroxyl species at the reaction sites is identified according to the Bader charge of hydroxyl oxygen with reference to those of H_2O_2 and H_2O[39].

Table S6. Bader charge analysis of chromium ions in key intermediates.

Species	Bader Charge/|e|	Valence
$Z[CrO_2]^+$	+1.54	+3
$Z[Cr(O)_2(OH)_2]^+$	+1.78	+6
$Z[CrO]^+$	+1.55	+3
CrO bulk	+1.13	+2
Cr_2O_3 bulk	+1.61	+3
CrO_3 bulk	+1.84	+6

We performed the Bader charge analysis to identify the valence state of the chromium cations in the key intermediates. As listed in **Table S6**, the Bader charges of key intermediates of $Z[CrO_2]^+$, $Z[Cr(O)_2(OH)_2]^+$, and $Z[CrO]^+$ are +1.54, +1.78, and +1.55 |e|. With reference to the Bader charges of Cr^{2+} in bulk CrO, Cr^{3+} in bulk Cr_2O_3, and Cr^{6+} in bulk CrO_3, the Cr^{3+}, Cr^{6+}, and Cr^{3+} are confirmed to respectively exist in $Z[CrO_2]^+$, $Z[Cr(O)_2(OH)_2]^+$, and $Z[CrO]^+$. The calculated results directly show that the valence of Cr at the initial and post-reaction sites is +3, which is consistent with the experimental results. As confirmed by the DFT simulation and experimental results, the active Cr species is hexavalent (Cr^{6+}) in the presence of H_2O_2. The Raman spectra indicate that the presence of H_2O_2 enables to efficiently oxidize the Cr^{3+} species to active Cr^{6+} species, which boosts the catalytic process of DOM over Cr_1/ZSM-5 SAC.

Supplemental References

1. Y. Lou, Y. Zheng, X. Li, N. Ta, J. Xu, Y. Nie, K. Cho and J. Liu, *J. Am. Chem. Soc.*, 2019, **141**, 19289-19295.
2. B. Qiao, J. Liu, Y.-G. Wang, Q. Lin, X. Liu, A. Wang, J. Li, T. Zhang and J. Liu, *ACS Catal.*, 2015, **5**, 6249-6254.
3. Y. Lou, Y. Cai, W. Hu, L. Wang, Q. Dai, W. Zhan, Y. Guo, P. Hu, X. M. Cao, J. Liu and Y. Guo, *ACS Catal.*, 2020, **10**, 6094-6101.
4. G. Kresse and J. Hafner, *Phys. Rev. B*, 1993, **47**, 558.
5. G. Kresse and J. Hafner, *Phys. Rev. B*, 1994, **49**, 14251.
6. J. P. Perdew, J. A. Chevary, S. H. Vosko, K. A. Jackson, M. R. Pederson, D. J. Singh and C. Fiolhais, *Phys. Rev. B*, 1992, **46**, 6671.
7. J. P. Perdew, K. Burke and M. Ernzerhof, *Phys. Rev. Lett.*, 1996, **77**, 3865.
8. S. Grimme, S. Ehrlich and L. Goerigk, *J. Comput. Chem.*, 2011, **32**, 1456-1465.
9. S. Grimme, J. Antony, S. Ehrlich and H. Krieg, *J. Chem. Phys.*, 2010, **132**, 154104.
10. A. Alavi, P. Hu, T. Deutsch, P. L. Silvestrelli and J. Hutter, *Phys. Rev. Lett.*, 1998, **80**, 3650.
11. P. J. Dauenhauer and O. A. Abdelrahman, *ACS Cent. Sci.*, 2018, **4**, 1235-1243.
12. M. Jørgensen, L. Chen and H. Grönbeck, *J. Phys. Chem. C*, 2018, **122**, 20351-20357.
13. T. P. Kaloni, *J. Phys. Chem. C*, 2014, **118**, 25200-25208.
14. X. Zhang, J. Wei, R. Li, C. Zhang, H. Zhang, P. Han and C. Fan, *J. Mater. Sci.*, 2018, **53**, 4494-4506.
15. H. Van Koningsveld, J. Jansen and H. Van Bekkum, *Zeolites*, 1990, **10**, 235-242.
16. S. R. Lonsinger, A. K. Chakraborty, D. N. Theodorou and A. T. Bell, *Catal. Lett.*, 1991, **11**, 209-217.
17. Z. Zhu, Z. Chang and L. Kevan, *J. Phys. Chem. B*, 1999, **103**, 2680-2688.
18. B. M. Weckhuysen, I. E. Wachs and R. A. Schoonheydt, *Chem. Rev.*, 1996, **96**, 3327-3350.
19. P. J. McCarthy, J. C. Lauffenburger, P. M. Skonezny and D. C. Rohrer, *Inorg. Chem.*, 1981, **20**, 1566-1570.
20. X. Xu, L. Liu, Y. Tong, X. Fang, J. Xu, D.E. Jiang and X. Wang, *ACS Catal.*, 2021, **11**, 5762-5775.
21. J. Gao, Y. Zheng, Y. Tang, J.-M. Jehng, R. Grybos, J. Handzlik, I. E. Wachs and S. G. Podkolzin, *ACS Catal.*, 2015, **5**, 3078-3092.
22. P. Stein, V. Miskowski, W. H. Woodruff, J. P. Griffin, K. G. Werner, B. P. Gaber and T. G. Spiro, *J. Chem. Phys.*, 1976, **64**, 2159-2167.
23. M. A. Vuurman, D. J. Stufkens, A. Oskam, J. A. Moulijn and F. Kapteijn, *J. Mol. Catal.*, 1990, **60**, 83-98.
24. F. Ayari, M. Mhamdi, D. P. Debecker, E. M. Gaigneaux, J. Alvarez-Rodriguez, A. Guerrero-Ruiz, G. Delahay and A. Ghorbel, *J. Mol.Catal. A: Chem.*, 2011, **339**, 8-16.
25. S. D. Yim, D. J. Koh, I. S. Nam and Y. G. Kim, *Catal. Lett.*, 2000, **64**, 201-207.
26. O. F. Gorriz and L. E. Cadús, *Appl. Catal. A*: Gen., 1999, **180**, 247-260.
27. C. Hammond, M. M. Forde, M. H. Ab Rahim, A. Thetford, Q. He, R. L. Jenkins, N. Dimitratos, J. A. Lopez-Sanchez, N. F. Dummer, D. M. Murphy, A. F. Carley, S. H. Taylor, D. J. Willock, E. E. Stangland, J. Kang, H. Hagen, C. J. Kiely and G. J. Hutchings, *Angew. Chem. Int. Ed.*, 2012, **51**, 5129-5133.
28. S. Bai, Y. Xu, P. Wang, Q. Shao and X. Huang, *ACS Catal.*, 2019, **9**, 6938-6944.

29. C. Williams, J. H. Carter, N. F. Dummer, Y. K. Chow, D. J. Morgan, S. Yacob, P. Serna, D. J. Willock, R. J. Meyer, S. H. Taylor and G. J. Hutchings, *ACS Catal.*, 2018, **8**, 2567-2576.
30. N. Agarwal, S. J. Freakley, R. U. McVicker, S. M. Althahban, N. Dimitratos, Q. He, D. J. Morgan, R. L. Jenkins, D. J. Willock, S. H. Taylor, C. J. Kiely and G. J. Hutchings, *Science*, 2017, **358**, 223-227.
31. Q. Shen, C. Cao, R. Huang, L. Zhu, X. Zhou, Q. Zhang, L. Gu and W. Song, *Angew. Chem. Int. Ed.*, 2020, **59**, 1216-1219.
32. T. Yu, Z. Li, W. Jones, Y. Liu, Q. He, W. Song, P. Du, B. Yang, H. An, D. M. Farmer, C. Qiu, A. Wang, B. M. Weckhuysen, A. M. Beale and W. Luo, *Chem. Sci.*, 2021, **12**, 3152-3160.
33. X. Tang, L. Wang, B. Yang, C. Fei, T. Yao, W. Liu, Y. Lou, Q. Dai, Y. Cai, X. M. Cao, W. Zhan, Y. Guo, X.-Q. Gong and Y. Guo, *Appl. Catal. B: Environ.*, 2021, **285**, 119827.
34. N. Yang, Y. Zhao, P. Wu, G. Liu, F. Sun, J. Ma, Z. Jiang, Y. Sun and G. Zeng, *Appl. Catal. B: Environ.*, 2021, **299**, 120682.
35. W. Huang, S. Zhang, Y. Tang, Y. Li, L. Nguyen, Y. Li, J. Shan, D. Xiao, R. Gagne, A. I. Frenkel and F. F. Tao, *Angew. Chem. Int. Ed.*, 2016, **55**, 13441-13445.
36. Y. Kwon, T. Y. Kim, G. Kwon, J. Yi and H. Lee, *J. Am. Chem. Soc.*, 2017, **139**, 17694-17699.
37. X. Cui, H. Li, Y. Wang, Y. Hu, L. Hua, H. Li, X. Han, Q. Liu, F. Yang, L. He, X. Chen, Q. Li, J. Xiao, D. Deng and X. Bao, *Chem*, 2018, **4**, 1902-1910.
38. M. H. Ab Rahim, M. M. Forde, R. L. Jenkins, C. Hammond, Q. He, N. Dimitratos, J. A. Lopez-Sanchez, A. F. Carley, S. H. Taylor, D. J. Willock, D. M. Murphy, C. J. Kiely and G. J. Hutchings, *Angew. Chem. Int. Ed.*, 2013, **52**, 1280-1284.
39. A. S. Rosen, J. M. Notestein and R. Q. Snurr, *Angew. Chem. Int. Ed.*, 2020, **132**, 19662-19670.